View metadata, citation and similar papers at core.ac.uk
brought to you by CORE
provided by NASA Technical Reports Server

CONTROL OF FORMATION-FLYING MULTI-ELEMENT SPACE INTERFEROMETERS WITH DIRECT INTERFEROMETER-OUTPUT FEEDBACK

Hui-Ling Lu and Victor H.L. Cheng
Optimal Synthesis Inc., 868 San Antonio Road, Palo Alto, CA 94303, USA.
and
Richard G. Lyon, and Kenneth G. Carpenter
NASA Goddard Space Flight Center, Greenbelt, Maryland 20771, USA.

ABSTRACT- *The long-baseline space interferometer concept involving formation flying of multiple spacecrafts holds great promise as future space missions for high-resolution imagery. A major challenge of obtaining high-quality interferometric synthesized images from long-baseline space interferometers is to accurately control these spacecraft and their optics payloads in the specified configuration. Our research focuses on the determination of the optical errors to achieve fine control of long-baseline space interferometers without resorting to additional sensing equipment. We present a suite of estimation tools that can effectively extract from the raw interferometric image relative x/y, piston translational and tip/tilt deviations at the exit pupil aperture. The use of these error estimates in achieving control of the interferometer elements is demonstrated using simulated as well as laboratory-collected interferometric stellar images.*

1. INTRODUCTION

The Hubble Space Telescope has been providing spectacular images of the cosmos for 15 years, and future space telescope concepts are being formulated to provide even more capable systems. To provide a larger effective aperture for producing higher-resolution imagery, many of these space telescope concepts are designed as space interferometers involving multiple optical elements flying far apart on separate spacecraft platforms in formation [1]–[3]. The designs allow the use of optical elements small enough for practical space launch to produce an effective aperture that is otherwise too large to be launched as a single monolithic optical element.

A major challenge of obtaining high-quality interferometric synthesized images from long-baseline space interferometers is to accurately control these spacecraft and their optics payloads in the specified configuration so that the optics would produce wavefront errors no more than $\lambda/14$ rms, i.e. diffraction limited.

Control of the optics traditionally depends on metrology sensors [4], [5] to provide the error signals required to determine the control required. For space interferometers that involve sub-wavelength accuracy of optics mounted on distributed platforms flying far apart in formation, the dependency on metrology sensors to provide error signals to the necessary level of accuracy would impose prohibitive cost and complexity requirements on their designs. Our research has focused on determining the optical errors to achieve fine control without resorting to additional sensing equipment. As a result, the concept reduces the complexity and cost of the control system by reducing or eliminating the requirements of other sensors and support infrastructure.

To ensure that the study will be realistic in addressing the underlying issues, the Stellar Imager (SI) mission [6] has been selected to provide the backdrop for defining the problem. The SI is a space interferometer concept that employs a large number of satellites as collectors for celestial imaging. As illustrated in Figure 1, it is a 0.5km-diameter UV-optical Fizeau interferometer made up of a configurable array of 10 to 30 1m-class spherical mirrors flying as "mirrorsats" and a central hub with focal-plane instrumentation. It is capable of providing an angular resolution of 60 μarcsec at 1550 Å, and 120 μarcsec at 2800 Å. Its goal is to image a substantial sample of nearby stars, with a resolution in the order of 1000 total pixels (~32 x 32) on a star's surface. NASA Goddard Space Flight Center (GSFC) has also developed the Fizeau Interferometer Testbed (FIT) [7], [8] for experimentations required to assess the SI concept.

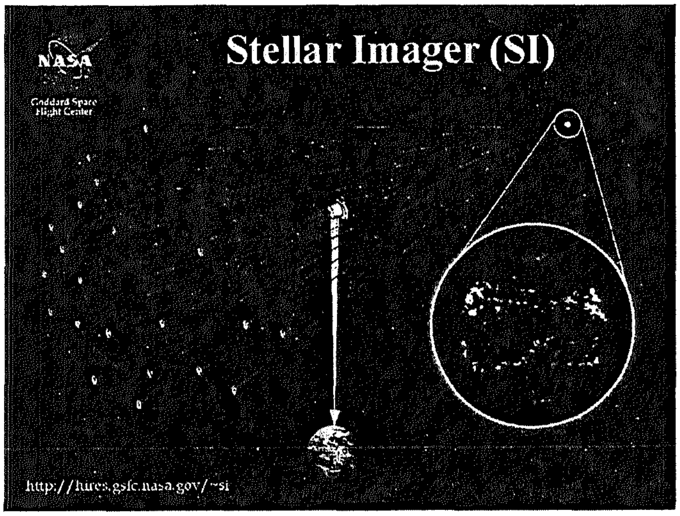

Figure 1. The Stellar Imager Mission Concept (Source [6])

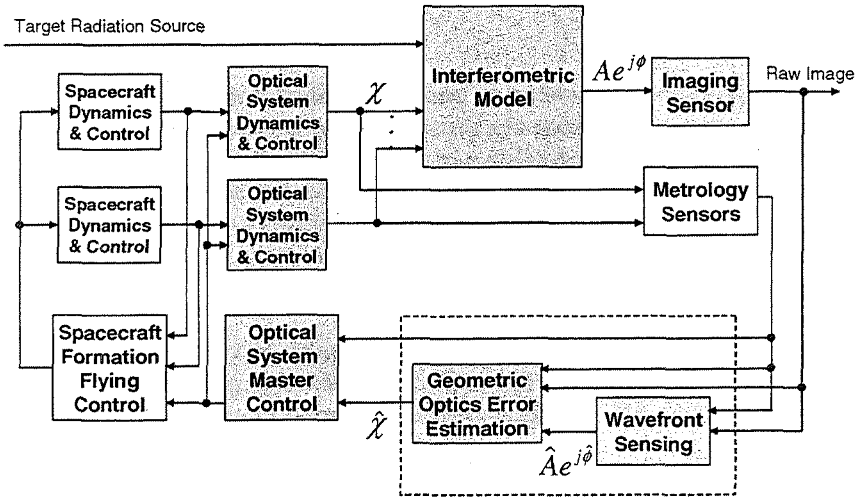

Figure 2. Control Concept Block Diagram

In order to achieve high-quality images under the SI mission, the position and orientation of the articulated mirrors need to be aligned precisely on the larger (0.5 km) virtual mirror surface to keep optical beams in phase. Each mirrorsat comes with 5 degrees of freedom of movement (tip, tilt, piston, as well as 2-D translations). The objective of our study is to control these mirrorsats using direct interferometer outputs. Figure 2 shows the overall control concept. Deviations of the mirrorsats, χ, from the desired mirror surface are estimated from direct interferometer outputs including the raw image collected at the central hub and other measurements from metrology sensors. The Optical System Master Control driven by estimated deviations and measurements from the metrology instrumentation issues commands to the optical system components on the separate spacecraft, as well as feeds back data to the Spacecraft Formation Flying Control. The Spacecraft Formation Flying Control in turn issues commands to control the collection of spacecraft. Furthermore, data from the optical system on each spacecraft is also fed back to the Optical System Master Control to modify the control decision in situations where the feedback of the estimated deviations is not adequate, e.g., when the actuators are hitting their limits.

Highly sophisticated wavefront estimation techniques—including those based on phase retrieval and phase diversity—already exist for determining the wavefront error [9], [10], [11], which when available can help to back out the errors of the optical elements. These techniques are essential for final processing of the data to convert the interferometer images to the desired stellar images, but they are very challenging computationally and they require extensive computational power and time. The objective behind our control concept is to investigate techniques that are useful for estimating the errors of the optical elements, with no requirement for complete online wavefront reconstruction. The rationale is, by relaxing the online wavefront-reconstruction requirement, more efficient techniques can be developed that impose lower computational requirements for deployment on spaceborne systems.

To this end, separate estimation techniques have been developed and verified for estimating the three classes of errors: x/y translational, piston, and tip/tilt. An integrated estimation/control procedure is also introduced to bring down the mirrorsat's deviations. The assessment of the algorithms developed has been based on simulated data as well as images collected by the FIT. The results establish the efficacy of the estimation algorithms in providing useful estimated data for the five degrees of freedom of mirror deviations for controlling the errors. In this paper, we will describe our estimation approaches, control strategy and evaluation results.

2. BACKGROUND MATERIAL ON OPTICAL SIGNAL PROCESSING

2.1. "Mirrorsat" Deviation and Interferometric Image

To infer deviations of the mirrorsats based on the collected raw images, the relationship between the geometric configuration of the mirrors and the observed image is considered in Figure 3. It is assumed that these spherical mirrorsats are configured and controlled under a predefined control coordinate system. Each mirror has 5 degrees of freedom: x, y, z (or piston) translation, and tip, tilt rotation. Geometric deviations of the mirrors are mapped into aperture deviations at the entrance pupil through a coordinate transformation. Under the assumption that there is perfect beam combination of the collected light beams from all the mirrors, the aperture configuration at the exit pupil would be a scaled version of the one at the entrance pupil [12]. This implies that geometric deviations of these spherical mirrorsats can also be obtained from the deviations of apertures at the exit pupil via a coordinate transformation. Deviations of the apertures include x, y, piston translational, and tip, tilt rotational errors. They are expressed by the wavefront error coordinate system [13], in which the piston variable points towards the nominal focal point of the optical system. These wavefront errors, at the exit pupil, are actual deviations from the ideal converging wavefront, i.e. the reference sphere; where the ideal wavefront would converge to an ideal focus at the detector plane. Thus, wavefront errors are the difference between the actual wavefront and the ideal wavefront at the system's exit pupil.

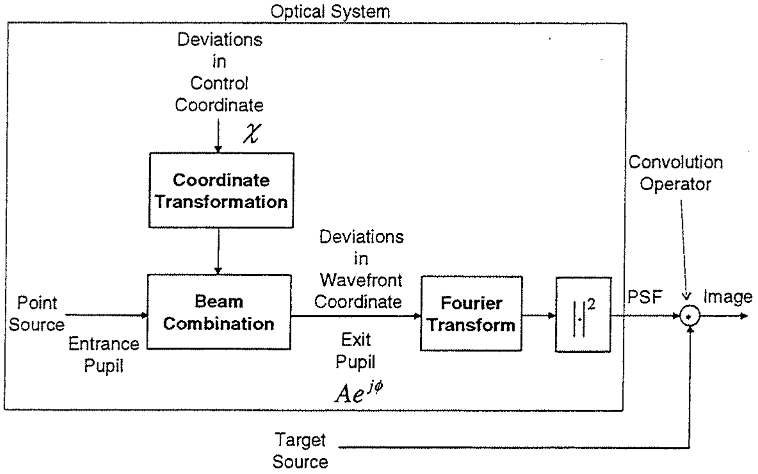

Figure 3. Optical System Modeling Showing Relationship between "Mirrorsat" Deviation and Interferometric Output Image

In the image domain, the properties of the optical system can be described by a point spread function (PSF), i.e. the image of an unresolved point source. The PSF is related to the wavefront errors (aka phase) at these exit pupil apertures through a Fourier transform [13]. More precisely, a PSF can be derived as the magnitude-squared of the Fourier transform of a complex pupil function Ae^{ϕ}. Deviations of exit pupil apertures are then shown as distortions from the ideal PSF. For a point source, an estimate of the PSF is readily obtained from the measured raw image on a sampled grid. In addition to the PSF, the modulation transfer function (MTF) defined as the magnitude of the Fourier Transform of the PSF, strehl ratio, and encircled energy are often used to evaluate properties of the optical system.

2.2. *Mathematical Imaging Model*

To support our data processing effort, we have adopted a mathematical imaging model [14] commonly used for describing optical systems. An observed noisy image, $d(x,y)$, can be represented as

$$d(x,y) = PSF(x,y;A,\phi) * o(x,y) + \eta(x,y) \tag{1}$$

where $PSF(x,y)$ is the optical point spread function, $o(x,y)$ is the object, and $\eta(x,y)$ is the noise, assumed additive but can actually consists of read noise, photon noise, flat-fielding errors etc. All functions are described in the (x, y) image plane coordinate.

From the principle of Fourier optics [14], PSF can be calculated from the two dimensional Fourier transform of complex pupil function:

$$PSF(x,y;A,\phi) = \left| \frac{1}{\lambda F} \iint A(u,v) e^{j\phi(u,v)} e^{-j2\pi\left(\frac{xu}{\lambda F} + \frac{yv}{\lambda F}\right)} du dv \right|^2 \tag{2}$$

The complex pupil function $P(u,v)$ is defined as $A(u,v)e^{j\phi(u,v)}$. $A(u,v)$ is the aperture mask function, which has value 1 where light passes through, and 0 otherwise. $\phi(u,v)$ is the phase delay at each point in the system exit pupil.[1] (u,v) are the spatial coordinates in the system exit pupil, λ is the wavelength of the monochromatic source, and F is the system focal length.

The optical transfer function (*OTF*) is the Fourier transform of the point spread function. If we define $u = \lambda F f_x$ and $v = \lambda F f_y$, *OTF* becomes

$$OTF = \frac{P \otimes P}{(P \otimes P)(0,0)} \tag{3}$$

where the symbol $\otimes$ represents the correlation operator.

3. ESTIMATION TECHNIQUES

3.1. *Estimation Techniques for x/y Translational Errors*

Here we present an estimation procedure that effectively extracts relative x/y translational exit pupil aperture deviations from the raw interferometric image with small estimation errors. The motivation of the proposed estimation technique is introduced, followed by the estimation procedure.

3.1.1. Problem Formulation

3.1.1.1. MTF and Baselines

To position the mirrorsats correctly, the baseline of each mirrorsat pair, defined as the separation of the pair's center locations at the exit pupil plane, needs to be maintained. It turns out that one can extract the baseline information from the MTF provided that the phase delay between the 2 apertures comprising the baseline pairs are within the coherence length of the passband, i.e. that they interfere.

---

[1] The system exit pupil limits the cone of rays from the image. It is defined as the image of the physical aperture looking from the image space through any optical elements between the aperture and the image plane.

A simple 2-element interferometer model can help explain the relationship between the MTF and the baseline. Figure 4 illustrates the PSF and MTF of a 2-element interferometer [15]. The 2-mirror PSF is a 1-mirror PSF modulated with fringes. The 1-mirror PSF is essentially the diffraction pattern of a single mirror. Assume that the size of the mirror is much smaller than the baseline of the interferometer, so that there are multiple fringe cycles within the 1-mirror PSF envelope. In the frequency domain, the MTF will consist of three distinct modes, which are observed as three dots in a pseudo-color depiction of the function. The base-band dot corresponds to the 1-mirror MTF and the other two are just translated versions of the 1-mirror MTF due to fringe modulation.

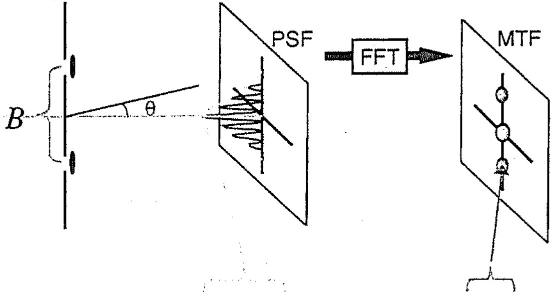

$$\underset{\text{Two Mirrors}}{PSF_{two}(\theta)} = 2\,\underset{\text{One Mirror}}{PSF_{one}(\theta)}\cdot[1+\cos(2\pi\cdot B/\lambda\cdot\theta)]$$

Figure 4. PSF and MTF of a 2-Element Interferometer

A Golomb configuration, which is considered by the SI mission, is an aperture configuration for sparse interferometric arrays optimized to minimize redundant baselines subject to the constraint that the apertures lie on a rectilinear grid. Figure 5 shows the MTF of a Golomb-7 configuration [16]. The simulated configuration consists of 7 circular apertures with diameter equal to 0.0125 m. The shortest baseline is 0.0254 m, which is about twice the diameter of each aperture. These baselines are large enough that the MTF dots are visibly separable. Since the spatial frequency of the fringes is related to the size and the direction of the baseline, the positions of these MTF dots contain information on the size and orientation of the baselines. Moreover, it is observed that the piston errors and the tip, tilt errors alter the shapes of the MTF dots, but they have little effect on the locations of their "centroids." Hence, under the assumption that baselines are larger than the diameter of individual mirrors and that the wavefront errors over an individual aperture are much less than the wavelength, baseline deviations can be estimated from the centroid deviations of the MTF dots. For a non-redundant constellation such as the Golomb configuration, the estimated baseline information can be used to estimate aperture deviations.

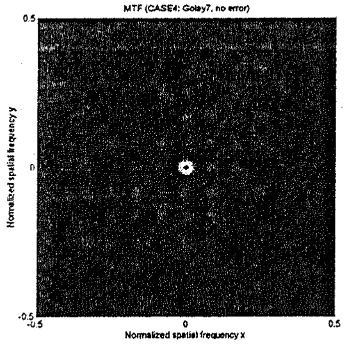

Figure 5. MTF of Golomb-7 Configuration

3.1.1.2. Baselines and Translational Deviations

In fact, the baseline error is a linear transformation of the x/y translational deviation. Let us define the baseline pattern $\bar{b}_i$ for the mirror *#i* as the collection of the MTF dots corresponding to all the baselines connected to the mirror *#i*. For example, Figure 6 shows the baseline patterns of the Golomb-7 configuration as red dots for individual mirrors.

If one numbers all positive MTF dots in sequence, the baseline pattern $\bar{b}_i$ can be denoted as a column vector, such as $[1 \ \ 0 \ \ 1 \ \ \ldots \ \ 0 \ \ 1]^T$, where 1's indicate all MTF dots corresponding to baselines connected to the mirror *#i*. Assuming that there are N mirrors and therefore $M = N\cdot(N-1)/2$ baselines, the relationship between the baseline error and the x/y translational deviation can be written as

$$[\bar{b}_1 \ \ \ldots \ \ \bar{b}_N]\begin{bmatrix}\Delta x_1\\ \vdots\\ \Delta x_N\end{bmatrix}=\begin{bmatrix}\Delta x'_1\\ \vdots\\ \Delta x'_M\end{bmatrix} \quad \text{or } A\cdot X = X' \tag{4}$$

where X represents the translational error in the exit pupil plane along the x axis, and X' represents the corresponding baseline error. (A similar formulation holds true for the y axis.) Since the MTF only retains the baseline information, matrix A has at most rank $N-1$; i.e., only $N-1$ independent variables can be recovered. One can reduce the number of independent variables by selecting a mirror as the reference mirror and estimating the relative deviations of other apertures with respect to the reference mirror. This process corresponds to

$$\begin{aligned} X' &= A\cdot X = [U_1 \quad U_2]\begin{bmatrix}\Sigma_1 & 0\\ 0 & 0\end{bmatrix}\begin{bmatrix}V_1^T\\ V_2^T\end{bmatrix}X = U_1\Sigma_1V_1^TX \\ &= U_1\Sigma_1\left[V_{11}^T \ \vdots \ V_{12}^T\right]\begin{bmatrix}0\\ \cdots\\ X_2\\ \vdots\\ X_N\end{bmatrix} = U_1\Sigma_1V_{12}^T\begin{bmatrix}X_2\\ \vdots\\ X_N\end{bmatrix} = A'\begin{bmatrix}X_2\\ \vdots\\ X_N\end{bmatrix}\end{aligned} \tag{5}$$

where $A' = U_1\Sigma_1V_{12}^T$ is a well-conditioned matrix of full rank $N-1$, and the relative aperture deviations can be obtained in the following equation by introduction of the pseudo-inverse.

$$[X_2 \ \ \cdots \ \ X_N]^T = (A'^TA')^{-1}\cdot A'^TX' \tag{6}$$

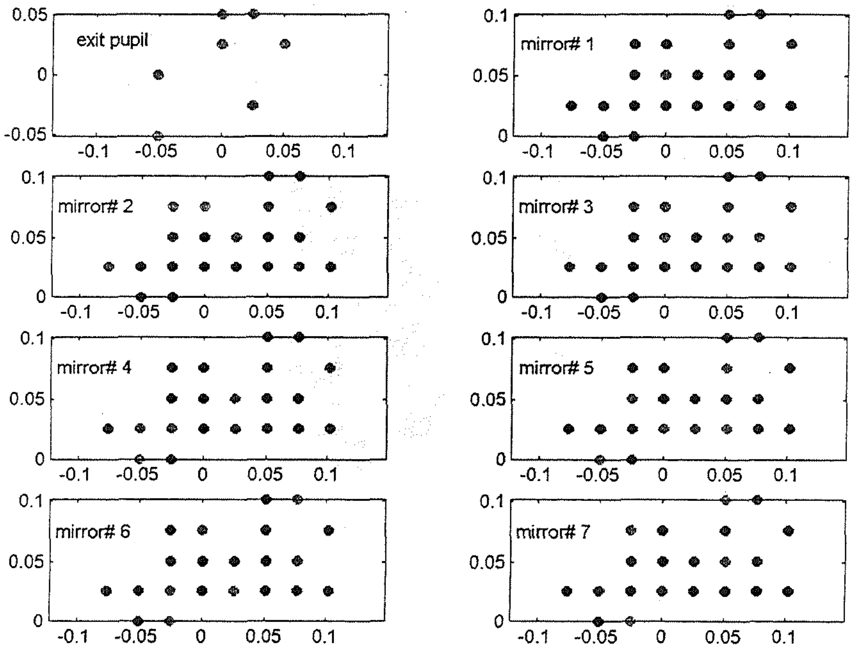

Figure 6. Baseline Patterns of Individual Mirrors

In summary, the centroid of an MTF dot is a prominent feature that has the potential to be used for determining the relative deviation of the center of the aperture on the exit pupil plane. However, with the only available raw image whose Fourier Transform is a noisy version of the true MTF, a robust centroid estimation algorithm is needed. The following section describes the overall estimation procedure that we have developed for extracting relative x/y translational aperture deviations from the raw interferometric image.

3.1.2. Estimation Procedure

An effective estimation procedure using a combination of a k-means clustering [17] technique and least-squares ellipse fitting [18], [19] is developed. The objective of the estimation is to calculate x/y translational deviations of exit pupil apertures so that every baseline is precisely maintained. Once every baseline is controlled at the predefined location, the PSF is known and the target image can be inverse-filtered from the measured raw image if there are no other deviations.

Figure 7 contains the flowchart of the estimation procedure [20]. In real measurements, the intensity observed at the focal plane contains photon noise, read-noise, dark current noise, flat fielding errors and stray light. The measurement model [8] can be expressed as

$$M(x,y;\alpha,flux,A,B,C) = flux \cdot PRF(x,y;\alpha) + A \cdot x + B \cdot y + C + \eta(x,y) \tag{7}$$

where PRF is the point response function, which is the intensity integrated across the spectral response and convolved with the detector spatial response function. In other words,

$$PRF(x,y;\alpha) = \int PSF(x,y;\alpha,\lambda)S(\lambda)d\lambda * rect\left(\frac{x}{\Delta x}\right)rect\left(\frac{y}{\Delta y}\right) \tag{8}$$

where $S(\lambda)$ is the source spectral radiance multiplied by the spectral transmission of the pass-band, and $rect\left(\frac{x}{\Delta x}\right)rect\left(\frac{y}{\Delta y}\right)$ is the wavelength-independent detector spatial response function.

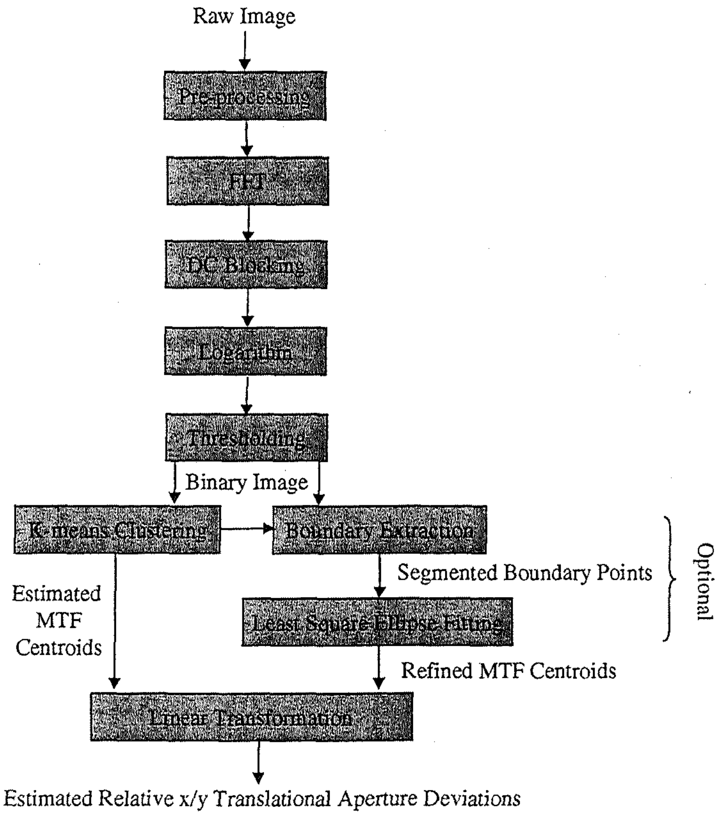

Figure 7. Estimation Procedure of the x/y Translational Deviations

With reference to Figure 7, the Pre-processing step removes the background terms in the measurement model. This is followed by the FFT where the Fourier Transform of the raw image is taken to approximate the MTF of the interferometric system. The DC Blocking removes the DC portion of the approximated MTF to amplify the MTF dots containing the baseline information. Since piston/tip/tilt deviations change the location of the intensity peak of some MTF dots, the Logarithm step in the estimation procedure is to reduce the dynamic range of the estimated MTF function so that reasonable thresholding results can be obtained. Afterwards, Thresholding is performed to convert the resulting image into a binary image. The thresholding value is selected by the criterion that 90% of the total energy is preserved. The next step of the estimation is to calculate the x/y translational deviations of the baselines from the thresholded binary image. Locations of the baselines are estimated as the center locations of the MTF dots. Three different methods have been tried to estimate the MTF centers: k-means clustering, direct least-squares ellipse fitting, and weighted least-squares ellipse fitting. Initialized with the desired baseline locations, k-means clustering estimates the centers of the MTF dots from binary image data points. One can further refine the center estimation of each MTF dot by the direct least-squares ellipse fitting or the weighted least-squares ellipse fitting method. Segmented boundary points belonging to different MTF dots are obtained via the boundary extraction and k-means clustering. Using these segmented data points, the ellipse fitting methods calculate the center of each MTF dot. The weighted least-squares ellipse fitting is a variation of the least-squares ellipse fitting, where each data point is weighted according to its MTF magnitude. Finally, with one aperture selected as the reference, deviations of the other apertures can be obtained from deviations of baselines through a linear transformation as shown in Eq. (6).

3.2. Estimation Techniques for Tip/Tilt Errors

3.2.1. Gradient Search Parametric Optimization

In this work, we have developed an effective estimation procedure for extracting small tip/tilt exit pupil deviations from interferometric images without estimating the wavefront error. The estimation is based on gradient search parametric optimization. The performance of the proposed estimation procedure achieves the angular peak wavefront error precision requirement $\lambda/4D$ (or equivalently $\pi/4$ in radian) almost all the time within a moderate number of iterations when the tip/tilt deviations are small.

Existing computational phase-diversity algorithms decompose the phase estimation problem into two sub-problems: object image reconstruction (equivalently, point-spread function estimation) and phase retrieval from the point-spread function. Due to the computational complexity of the phase-diversity methods, our research has focused on alternatives to estimate piston/tip/tilt exit-pupil deviations without estimating the image object explicitly, which is not required for the purpose of estimating the optical error for controlling the interferometer's operations. Since our objective is to obtain estimates of piston/tip/tilt exit-pupil deviations, the phase of the complex pupil function is parameterized by the Zernike polynomials for each exit pupil and the coefficients of the first three Zernike modes represent the piston, tip and tilt, respectively. Towards this end, we have developed a tip/tilt parametric estimation method based on gradient search which minimizes an objective function that does not require the information of the imaging object source.

Recall from Section 2.2, that the measured raw image $d(x,y)$ in the spatial domain can be modeled as the convolution result of the imaging source $o(x,y)$ and the point-spread function (PSF) of the optical system, i.e.,

$$d(x,y) = PSF(x,y;A,\phi) * o(x,y) + \eta(x,y), \qquad (9)$$

where PSF is the magnitude square of the Fourier transform of the complex pupil function $Ae^{j\phi}$, and $\eta(x,y)$ is the noise often modeled as Gaussian white noise. In the frequency domain, we can represent the imaging model as $D(f_x,f_y) = OTF(f_x,f_y)\cdot O(f_x,f_y) + H(f_x,f_y)$. In this work, we assume that one pair of images with known phase diversity are available. For example, let $d_1 = PSF(\phi) * o + \eta_1$ denote the original image and $d_2 = PSF(\phi+\theta) * o + \eta_2$ denote the phase-diversed image with known phase aberration θ added. There are two practical ways to introduce the phase diversity: changing the detector focal position or changing the imaging wavelength. Here, the phase-diversed image is introduced by defocusing. In the frequency domain and under the no-noise condition, we can write $D_1(f_x,f_y) = OTF_1(f_x,f_y) \cdot O(f_x,f_y)$ and $D_2(f_x,f_y) = OTF_2(f_x,f_y) \cdot O(f_x,f_y)$.

It can be observed that $D_1(f_x,f_y) \cdot OTF_2(f_x,f_y) - D_2(f_x,f_y) \cdot OTF_1(f_x,f_y) = 0$. Hence, we can choose the objective function to be

$$f(\vec{a},\vec{b},\vec{c}) = \sum_{f_x}\sum_{f_y}\left|D_1(f_x,f_y) \cdot O\hat{T}F_2(f_x,f_y) - D_2(f_x,f_y) \cdot O\hat{T}F_1(f_x,f_y)\right|^2 \tag{10}$$

The estimated OTF is represented as $FFT\left(\left|FFT\left(\sum_{i=1}^{N} A_i e^{j\left(a_i + b_i(x - x_i^c) + c_i(y - y_i^c)\right)}\right)\right|^2\right)$ where N is the number of mirrors, A_i is the masking function for the ith exit-pupil aperture, (x_i^c, y_i^c) is the aperture center of the ith exit-pupil aperture, $\vec{a} = [a_1 \ \cdots \ a_N]$ denotes the piston deviations, $\vec{b} = [b_1 \ \cdots \ b_N]$ denotes x-tilt (tip) deviations, and $\vec{c} = [c_1 \ \cdots \ c_N]$ denotes the y-tilt (tilt) deviations. The same objective function was also used in Harikumar's [21] work on blind restoration of images blurred by multiple filters. In summary, the piston/tip/tilt estimation can be formulated as an unconstrained nonlinear optimization problem:

$$\text{Minimize } f(\vec{a},\vec{b},\vec{c}) = \sum_{f_x}\sum_{f_y}\left|D_1(f_x,f_y) \cdot O\hat{T}F_2(f_x,f_y) - D_2(f_x,f_y) \cdot O\hat{T}F_1(f_x,f_y)\right|^2 \tag{11}$$

over. $(\vec{a},\vec{b},\vec{c})$

Nonlinear optimization problems can be solved by local gradient search type method or global search method such as genetic algorithm. Since global search methods are in general computationally expensive, the local gradient search method is preferred when the error surface of the optimization problem is convex-like.

In order to understand the convergence property of the gradient approach for our application, error surfaces were examined. We observed that all error surfaces near the solution (approximately within $\pm\pi$ range of the solution) are convex-like, which ensures a fast convergence and unique solution when the initial guess is approximately within the $\pm\pi$ range of the solution.

By comparing the value of the objective functions for the case of the presence or absence of the piston deviations using the monochromatic simulation program, we also found that the piston deviations have little impact on the value of the objective function based on defocusing phase diversity. Therefore, we can neglect the biases resulting from the piston deviations when estimating the tip/tilt deviations. This fact ensures that we can estimate the tip/tilt deviations without the knowledge of piston deviations with sufficient defocusing diversity present.

3.2.2. Estimation Using Unconstrained Gradient-Search Optimization

With a maximum of 30 mirrorsats present in the SI mission, the total number of optimization variables are no larger than 60 for tip/tilt estimation. This can be considered a medium-scale optimization problem. The BFGS Quasi-Newton method with a mixed quadratic and cubic line search procedure can be used to find optimal solutions of tip/tilt deviations. Since the computational complexity is high to perform the analytic gradient calculation. Gradients are approximated via finite differencing. The BFGS formula is used to update the approximation of the Hessian matrix. Due to the well-behaved error surface, the tip/tilt estimates can converge to the correct solutions within a few iterations when the deviations are within the convex range. In general, the performance of the tip/tilt estimation decreases when the tip/tilt deviations are increased. The performance of the tip/tilt deviations can be inferred from the 2-norm of the estimated results. An empirical threshold has been derived to determine whether control should be applied according to the estimated results.

3.2.3. Estimation Using Sequential Unconstrained Minimization Technique

In addition to the unconstrained optimization method with performance indexing, alternatively, we have also developed an estimation procedure based on the sequential unconstrained minimization technique (SUMT) [22]. The motivation is that we would like to constrain the estimates to be bounded within the convex range of the error surface by assuming that the tip/tilt deviations are small and are within the convex range also. We have assumed that the convex range for tip/tilt deviations is $\pm\pi$ through empirical study of the error surfaces. By introducing the bounds on the optimization variables, our optimization problem can be formulated as follows:

$$\text{Minimize } f\,(0,\bar{b},\bar{c}) \qquad (12)$$
$$\text{Subject to } \bar{b}-\pi<0,\ -\bar{b}-\pi<0,\ \bar{c}-\pi<0, \text{ and } -\bar{c}-\pi<0.$$

where f is defined in Eq (11), $\bar{b}$ denote the tip deviations and $\bar{c}$ denote the tilt deviations. SUMT is applied to solving the above equation. The basic concept behind SUMT is to solve a sequence of smooth unconstrained problems by transforming the constraints into a smooth barrier function.

3.3. Estimation Techniques for Piston Error

Although we have used the technique of phase diversity via defocusing for tip/tilt estimation, it turns out not to be a suitable technique for the piston estimation. The error surfaces with respect to piston deviations are highly nonlinear with multiple minima which contain 2π ambiguities relative to the desired pistons. Instead, wavelength diversity method is introduced to directly eliminate the 2π-ambiguity problem in piston estimation.

Phase ambiguity in monochromatic piston estimation is a well-known problem. Motivated by the concept that the effective wavelength can be extended by two wavelengths (i.e., $\lambda_e = \lambda_1\lambda_2 / (\lambda_2-\lambda_1)$), our technique extends the previously developed parametric optimization scheme to incorporate wavelength diversity with the intent to directly estimate piston deviations without resolving the phase ambiguity separately. In short, the estimation problem of piston deviation is formulated as a nonlinear parametric estimation problem which minimizes an objective function of the form $\sum_{f_x}\sum_{f_y}\left|D_1(f_x,f_y)\cdot OT\hat{F}_2(f_x,f_y)-D_2(f_x,f_y)\cdot OT\hat{F}_1(f_x,f_y)\right|^2$ over the parameter spaces of piston positions. Here, $D_1(f_x,f_y)$ is the frequency response of the raw interferometric image measurement with wavelength λ_1, $D_2(f_x,f_y)$ is the frequency response of the raw interferometric image measurement with wavelength λ_2, $OT\hat{F}_1(f_x,f_y)$ is the estimated optical transfer function with wavelength λ_1 and $OT\hat{F}_2(f_x,f_y)$ is the estimated optical transfer function with wavelength λ_2.

Another advantage of constructing the objective function using wavelength diversity is that the piston estimates are not sensitive to the masking function estimation errors at all.

We again use SUMT to solve the piston optimization problem. The surface of the objective function is lifted up through SUMT [22] where we deliberately constrain the optimization searching space to be within the valid piston range, assuming that the piston deviations are within the extended non-ambiguous region. In this case, local minima can be eliminated. For estimation of the piston deviations, only relative piston errors are observable at the interferometric raw images. Therefore, the resulting piston estimates for all apertures are offset to get rid of the global piston error across all apertures.

3.4. Integrated Estimation/Control Procedure

As a result of the lessons learnt as documented in the previous sections, we propose an integrated estimation/control procedure that would (i) estimate the tip/tilt deviations using two images with phase diversity via defocusing, and (ii) to estimate the piston deviations using two images with wavelength diversity. The piston deviations have very little impact on the estimation of tip/tilt deviations, whereas the tip/tilt deviations would introduce biases on the piston estimations. These facts lead us to the integrated procedure to achieve the control accuracy requirements of the piston/tip/tilt deviations.

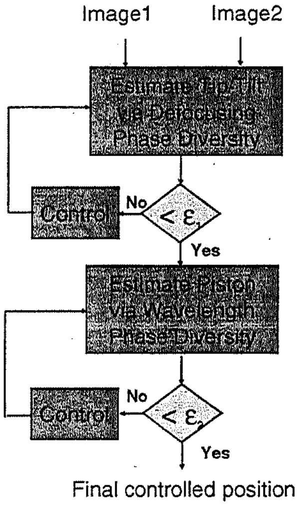

$$\lambda_e = \frac{\lambda_1 \lambda_2}{\lambda_2 - \lambda_1}$$

Figure 8. Integrated Estimation/Control Procedure

Figure 8 shows the integrated estimation/control procedure. First, the tip/tilt deviations are estimated and controlled iteratively until the tip/tilt deviations are below some pre-specified threshold at which the piston estimation biases is tolerable, and the tip/tilt deviations are below the control accuracy requirement. Subsequently, the piston deviations are estimated and controlled iteratively until the piston deviations satisfy the piston accuracy requirement. This estimation/control procedure works well and efficiently when the piston/tip/tilt deviations are small enough to be within the convex region. When the deviations are large, the objective function is no longer convex and multiple minima exist for the tip/tilt estimation. Global optimization methods are needed to extend the estimation range.

4. RESULTS AND DISCUSSION

Two data sources have been used to evaluate the estimation and control schemes: data generated by computer simulations of the optics, and data collected from the FIT. The computer simulated raw image was calculated by convolving a model image of the Sun in the light of CIV atoms (1550 Å transitions) with the point spread function generated using the Golomb-7 configuration. The Fizeau Interferometer Testbed (FIT) [7], [8] is a ground-based experimental system developed at NASA GAFC to support the development and validation of technologies relevant to SI and other space-based interferometry missions. The FIT data set was collected with the aperture configuration of Golomb-7. All the data had been collected using point-source filtering with two different 80-nm narrow-band filters centered at wavelengths of 600 nm and 700 nm. The CCD detector of the FIT has resolution of 16 bits and the physical dimension of each pixel is 9 μm.

4.1. Evaluation of Estimation and Control Functions for exit-pupil x/y translational Errors

Here we present the statistical evaluation results based on the dataset collected from the FIT. The evaluation results for computer simulated images have been presented elsewhere [20]. For this assessment, the bias and variance of the estimation procedure are calculated. Our evaluation also includes investigation of the impact of other actuator deviations, such as tip/tilt and piston deviations, on the performance of the x/y translational estimation algorithm.

Here, Table 1–Table 2 tabulate the average estimation errors and the standard deviations of the estimation procedure using k-means clustering, least-square ellipse fitting or the least-square weighted ellipse fitting methods. The input images are collected with source wavelength of 700 nm (± 20 nm) and 600 nm (± 20 nm). The two numbers in each cell of the tables correspond to quantities in the x and y directions.

Table 1. Average Estimation Error of x/y Translational Deviations (in cm)

Wavelength\Method	k-Means Clustering	Ellipse Fitting	Weighted Ellipse Fitting
700 nm	0.0157/0.0224	0.0168/0.0229	0.0161/0.0229
600 nm	0.0188/0.0530	0.0189/0.0531	0.0187/0.0533

Table 2. Standard Deviation of x/y Translational Deviations Estimation (in cm)

Wavelength\Method	k-Means Clustering	Ellipse Fitting	Weighted Ellipse Fitting
700 nm	0.0073/0.0092	0.0129/0.0110	0.0084/0.0095
600 nm	0.0097/0.0093	0.0097/0.0104	0.0098/0.0109

To study the impact of mirror piston/tip/tilt deviations on the proposed estimation procedure, Table 3 summarizes the average estimation errors of the x/y translational deviation estimation for dataset without perturbation, tip/tilt perturbations[2], and piston perturbations. In these two tables, data from both wavelengths have been combined. In general, piston/tip/tilt perturbations of mirrors do not impact the average estimation error. It indicates that our estimation method is robust to mirror deviations. Comparing the estimation results using k-Means clustering with the further refinement results using ellipse fitting methods, we do not observe the further improvements. All in all, k-means clustering method provides efficient yet effective estimation results.

Table 3. Average Estimation Error of x/y Translational Deviations (in cm) for Perturbation Comparisons

Method▶ ▼Perturbation Source	k-Means Clustering	Ellipse Fitting	Weighted Ellipse Fitting
Nominal	0.0171/0.0374	0.0181/0.0376	0.0177/0.0374
Piston	0.0173/0.0404	0.0176/0.0410	0.0175/0.0410
Tip/tilt	0.0173/0.0381	0.0178/0.0382	0.0173/0.0385

4.2. Evaluation of Estimation and Control Functions for Tip/Tilt Errors

To reassure the effectiveness of the proposed tip/tilt estimation procedure, statistical performances of x-tilt and y-tilt estimations using both unconstrained gradient optimization method and SUMT are summarized here. The average errors shown here are the root-mean-square estimation errors across all mirrors. Golomb-7 configuration is used to simulate one pair of phase-diversity images. The simulated Sun image is used to serve as the extended source. X-tilt deviations are generated by uniform noise generator with maximum deviations ranging from $\pi/4$ to 4π.

Table 4 shows the average estimation errors for unconstrained gradient optimization method excluding the bad estimates where the 2-norm of the estimated tip/tilt deviations is larger than the empirical threshold. When the empirical rule is applied to the tip/tilt estimations, the tip/tilt estimation results meet the rotational precision requirement if the maximum scale of the uniformly distributed tip/tilt deviations is no larger than 2π.

Table 4. Tip/Tilt Average Estimation Error

Deviation▶ ▼Imaging Source	$\pi/2$	π	2π	3π	4π
Point Source	0.0015	4.0451e-4	0.5038	1.3904	2.7874
Extended	0.0751	0.1510	0.4010	2.1243	3.1393

---

[2] Due to the mounting of these actuators, small piston deviations are inevitable.

In the previous results, we have assumed that the defocusing amount of the phase-diversed image is known. In reality, however, we would probably only have knowledge of its approximate value. We would then need to estimate the defocusing amount along with the tip/tilt deviations. Table 5 summarizes the average estimation errors for the case of joint estimation excluding bad estimates according to the empirical rule that we derived, as given by the first number in each cell. For comparison with the average estimation error for joint estimation, each cell also includes a second number representing the average estimation error when only tip/tilt deviations are estimated. These data reveal the degree of performance deterioration due to the lack of prior knowledge in the defocusing amount.

We have also studied the use of SUMT as an alternative optimization method. All of the optimization variables (tip/tilt deviations in this case) are constrained to be within ±3π. We observe that the average estimation errors via SUMT are comparable to the results in Table 6 using unconstrained gradient search method with outlier excluded.

Table 5. Tip/Tilt Average Estimation Error for Joint Estimation

Deviation ▶ **▼Imaging Source**	π/2	π	2π	3π
Point Source	0.001587/ 4.0463e-5	0.001779/ 4.1761e-5	0.22045/ 0.2203747	0.53189/ 0.493030
Extended	0.008147/ 0.003007	0.71257/ 0.51776	0.9154/ 0.63074	0.9413/ 2.9270e-5

Table 6. Tip/tilt Average Estimation Errors via SUMT

Deviation ▶ **▼Imaging Source**	π	2π	3π
Point Source	0.00568	0.04694	1.1579
Extended	0.039213	0.4208	2.26801

4.3. Evaluation of Estimation and Control Functions for Piston Errors

The piston estimation method is via wavelength diversity and SUMT. Here, we assess the technique through examination of statistical results in terms of average piston estimation errors. The input data are generated using our monochromatic interferometer simulation program under the Golomb-7 configuration. According to the calibration data collected by FIT, two images are simulated using wavelengths of 600 nm and 700 nm for each run of the piston estimation. Here, the effective wavelength is 4200 nm, that is, seven times of 600 nm. We therefore set the constraint on the piston optimization variables to be ±3.5λ.

Table 7. Average Piston Estimation Errors (Extended Source)

Tilt Deviation ▶ **▼Piston**	**0**	**π/12**	**π/6**	**π/4**	**π/3**	**5π/12**
2π	0.4722	0.55078	0.89816	1.16549	1.39181	1.585805
4π	0.462948	0.4689	0.97264	1.17298	1.3661961	1.645779
6π	0.410226	0.70546	0.93671	1.190100	1.443579	1.75521
8π	4.27170	4.3481	4.310285	5.16525116	2.966947	4.88295

Table 7 summarizes the results when one snapshot of the Sun image was taken as the extended source. The piston deviations are uniformly distributed between ±2π, ±4π, or ±6π. To study the impact of the tip/tilt deviations on the piston estimation, the tip/tilt deviations are also uniformly distributed between 0 (no deviations), ±π/12, ±π/6, ±π/4, ±π/3, ±5π/12, or ±π/2. Tip/tilt deviations impact the piston estimation performance negatively. The average piston estimation errors increase for larger tip/tilt deviations. The average piston estimation errors also mostly increase when the piston deviations increase and the estimation results are not reliable once the piston deviations are larger than the ±7π constraint.

4.4. Evaluation of the Integrated Estimation/Control Procedure

Figure 9 demonstrates the effectiveness of the proposed integrated estimation/control procedure by showing four iterations of the procedure. In each case, the left-hand side of the figure shows the exit-pupil phase errors and the right-hand side of the figure shows the corresponding simulated point spread function. In this example, the initial piston/tip/tilt deviations $\Delta\mathbf{x}$ in radians for the apertures are represented by the following matrix

$$\begin{bmatrix} 1.5339 & 7.4507 & -4.9294 & 5.3658 & -8.7590 & 4.2856 & -4.9476 \\ 2.9538 & 3.3587 & -1.1351 & -1.5461 & 1.6299 & 1.7948 & -3.3580 \\ 0.4467 & -1.8781 & -0.5904 & 2.3107 & 3.5102 & -1.8787 & 3.8617 \end{bmatrix}$$

where the first row is the piston deviation, the second row is the x-tilt deviation and third row is the y-tilt deviation. Each column of the matrix corresponds to one aperture.

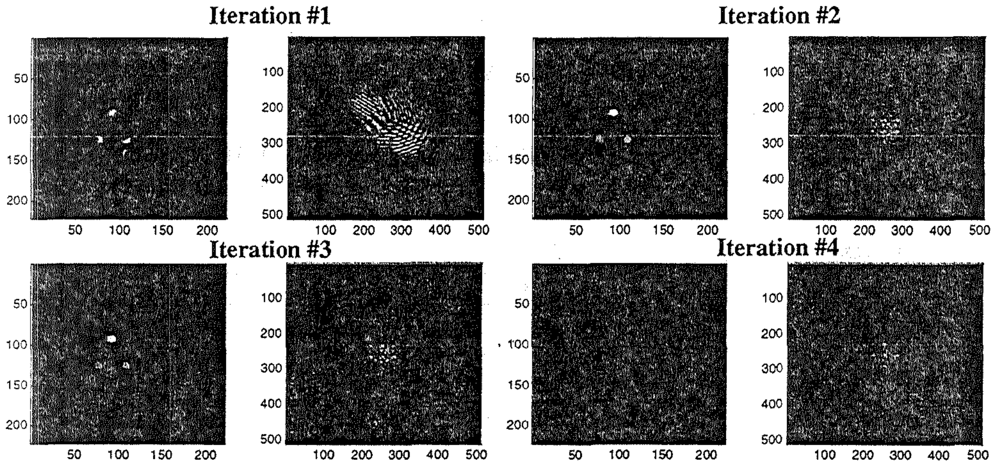

Figure 9. Integrated Estimation/Control Example

The tip/tilt deviations are corrected during the first three iterations and the piston deviations are corrected during the last iteration. In this example, the final exit-pupil phase errors are almost zero and the point spread function is well aligned. At the last iteration, the magnitude of the maximum piston deviations is 0.00022 radian, the magnitude of the maximum x-tilt deviations is 0.0000316 radian and the magnitude of the maximum y-tilt deviations is 0.0000055 radian.

5. CONCLUDING REMARKS

This study is concerned with the development of estimation techniques for determining the errors in the optical configurations of space interferometers without depending on prohibitively expensive metrology instrumentation. The idea is to extract the necessary error information from the raw images collected by the interferometer. To ensure that the study will be realistic in addressing the underlying issues, the Stellar Imager (SI) mission has been selected to provide the backdrop for defining the problem.

To this end, separate estimation techniques have been developed and verified for estimating the three classes of errors: x/y translational, piston, and tip/tilt. The assessment of the algorithms developed has been based on simulated data as well as images collected by the FIT. The results establish the efficacy of the estimation algorithms in providing useful estimated data for the five degrees of freedom of mirror deviations for controlling the errors, and this has been demonstrated for seven mirrors in a Golomb-7 configuration. Future research is recommended for further testing and refinement of these algorithms in a physical laboratory setting.

6. REFERENCES

[1] P. R. Lawson (Ed.), *Selected Papers on Long Baseline Stellar Interferometry*, SPIE Milestone Series, Vol. MS 139, SPIE, 1997.

[2] R. D. Reasenberg, *Astronomical Interferometry, Proceedings of SPIE*, Vol. 3350, Kona, HI, March 20–24, 1998.

[3] R. D. Reasenberg, *Spaceborne Interferometry II, Proceedings of SPIE*, Vol. 2477, Orlando, FL, April 19–20, 1995.

[4] Y. Gürsel, "Metrology for Spatial Interferometry," *Amplitude and Intensity Spatial Interferometry II, SPIE Proceedings*, Vol. 2200, Kona, HI, March 15–16, 1994, pp. 27–34.

[5] Y. Gürsel, "Metrology for Spatial Interferometry II," *Spaceborne Interferometry II, SPIE Proceedings*, Vol. 2477, Orlando, FL, April 19–20, 1995, pp. 240–258.

[6] K. G. Carpenter, C. J. Schrijver, M. Karovska, and the SI Vision Mission Study Team, "The Stellar Imager (SI) Vision Mission," *SPIE Astronomical Telescopes and Instrumentation*, May 24-31, 2006, Orlando, FL, *SPIE* Paper #6268-77.

[7] Zhang, X., K. Carpenter, R. Lyon, H. Huet, J. Marzouk, and G. Solyar, "The Fizeau Interferometry Testbed," *IEEE Conference*, Bigsky Montana, Mar. 2003.

[8] Lyon, R. G., et al, "Fizeau Interferometry Testbed: Wavefront Control," *SPIE Astronomical Telescopes and Instrumentation*, June 21-25, 2004, Glasgow Scotland, *SPIE Paper* #5487_37.

[9] Gonsalves, R. A., "Phase Retrieval and Diversity in Adaptive Optics," *Optical Engineering*, Vol. 21, pp. 829–832, 1982.

[10] Lyon, R. G., J. E. Dorband, T. Murphy, G. Solyar, "Overview: Computational Complexity and Space Based Optical Systems," *Proceedings of the Workshop on Computational Optics and Imaging for Space Applications,* pp. 102–115, NASA Goddard Space Flight Center, May 10–12, 2000.

[11] Luke, D. R., J. V. Burke, and R. G. Lyon, "Optical Wavefront Reconstruction: Theory and Numerical Methods," *SIAM Review*, Vol. 44, pp. 169–224, 2002.

[12] J. E. Harvey, P. R. Silverglate, and A. B. Wissinger, "Optical performance of synthetic aperture telescope configurations," *Southwest Conference in Optics*, pp. 110–118, *SPIE* Vol. 540, 1985.

[13] W. Goodman, *Introduction to Fourier Optics*, McGraw-Hill Inc., 1996.

[14] Banham, M. R., and A. K. Katsaggelos, "Digital Image Restoration," *IEEE Signal Processing Magazine*, pp. 24–41, Mar. 1997.

[15] Chung, S.-J., "Design, Implementation and Control of a Sparse Aperture Imaging Satellite," *Master of Science Thesis*, Department of Aeronautics and Astronautics, MIT, 2002.

[16] Golomb, S. and Taylor, H., "Two-dimensional synchronization patterns for minimum ambiguity," *IEEE Trans. on Info Theory.*, Vol. 28, No. 4, pp. 600–604, 1984.

[17] Corney, D., "the Clustering toolbox," Computer Science Dept., University College London, 2000. (http://www.cs.ucl.ac.uk/staff/D.Corney/ClusteringMatlab.html, March 2005)

[18] Fitzgibbon, M. Pilu , R. Fisher, "Direct least-square fitting of Ellipses," *IEEE Trans. on Pattern Analysis and Machine intelligence*, Vol. 21, No. 5, May 1999.

[19] Halíř, R., and J. Flusser, "Numerically stable direct least squares fitting of ellipses," *In the 6th Int. Conf. in Central Europe on Computer Graphics and Visualization.*, Plzen, Czech Republic, 1998.

[20] Lu, H.-L., V. H. L. Cheng, J. A. Leitner, R. G. Lyon, and K. G. Carpenter, "Estimation of Aperture Errors with Direct Interferometer-Output Feedback for Spacecraft Formation Control," *Proc. American Control Conference*, pp. 4090–4095, 2004.

[21] Harikumar, G., and Y. Bresler, "Exact Image Deconvolution from Multiple FIR Blurs," *IEEE Trans. on Image Processing*, Vol. 8, No. 6, pp. 846–862, June 1999.

[22] Boyd, S., and L. Vandenberghe, *Convex Optimization*, Cambridge University Press, 2003.